



Article

Rice Crop Monitoring Using Sentinel-1 SAR Data: A Case Study in Saku, Japan

Shoko Kobayashi ^{1,*} and Hiyuto Ide ²¹ College of Agriculture, Tamagawa University, Tokyo 194-8610, Japan² Sharagri Company, Tokyo 102-0093, Japan; hiyuto.ide@sharagri.com

* Correspondence: kshoko@agr.tamagawa.ac.jp

Abstract: Global warming affects rice crop production, causing deterioration of rice grain quality. This study used C-band microwave images taken by the Sentinel-1 satellites to monitor rice crop growth with the aim to understand microwave backscatter behavior, focusing on decreases in panicle water contents with ripening, which affect C-band backscatter. Time-series changes illustrated a similar tendency across all four analysis years, showing that VV/VH ratio at an incidence angle of 45–46° stopped decreasing to be stable over the reproductive and ripening periods due to reductions in the panicle water content that allowed for greater microwave penetration into the canopy, thereby increasing panicle-related backscatter. Furthermore, multivariate regression analysis combined with field observations showed that VV and VH with the shallow incidence angles were significantly negatively correlated with panicle water content, which well demonstrated backscatter increases with plant senescence. Furthermore, it was observed that backscatter behaviors were highly consistent with changes in crop phenology and surface condition. Accordingly, Sentinel-1 images with shallow incidence angles and high revisit observation capabilities offer a strong potential for estimating panicle water content. Therefore, it seems reasonable to conclude that C-band SAR data is capable of retrieving grain filling conditions to estimate proper harvesting time.

Keywords: rice growth; synthetic aperture radar; sentinel-1; crop phenology; canopy; panicle water contents; microwave satellite



Citation: Kobayashi, S.; Ide, H. Rice Crop Monitoring Using Sentinel-1 SAR Data: A Case Study in Saku, Japan. *Remote Sens.* **2022**, *14*, 3254. <https://doi.org/10.3390/rs14143254>

Academic Editors: Francisco Javier Mesas Carrascosa and Andrés Felipe Ríos Mesa

Received: 20 May 2022

Accepted: 29 June 2022

Published: 6 July 2022

Publisher's Note: MDPI stays neutral with regard to jurisdictional claims in published maps and institutional affiliations.



Copyright: © 2022 by the authors. Licensee MDPI, Basel, Switzerland. This article is an open access article distributed under the terms and conditions of the Creative Commons Attribution (CC BY) license (<https://creativecommons.org/licenses/by/4.0/>).

1. Introduction

Rice is a staple food and maintains the highest self-sufficiency rate among the other agricultural products in Japan. In addition, it serves as a major food source for over half of the world's population [1].

The detrimental impacts of global warming on crop cultivation, including high-temperature damages to plants known as heat stress, have become too large to ignore and must be assessed concerning productivity and food security [2]. The Ministry of Agriculture, Forestry and Fisheries of Japan pointed out the issue about 15 years ago, and numerous local governments have issued a strong warning about the damage to farmers in recent years [3]. Rice crops are particularly susceptible to heat, leading to stress and deteriorating grain quality primarily through cracked grains or white immature grains, which are triggered by high temperatures during the early grain-filling period [1,4]. Accordingly, harvesting should be conducted immediately after grain-filling to avoid exposing the plant to heat stress. Particularly, it is well known that water content in paddy rice excessively decreases by delayed harvest, which causes cracked grains. Thus, estimating the optimum harvesting timing is an urgent issue that needs to be solved. In Japan, optimum harvesting timing is traditionally determined via field observations by local or regional governments and is calculated based on accumulated average daily air temperatures after the heading [5].

In general, the rice growing stage begins with the vegetative stage, which includes transplanting and tillering, which refers to the development of several stems on one plant [6].

After reaching maximum tiller number, the panicle initiation and heading, which indicates panicle exertion out of the end of the stem, start, followed by flowering and ripening stages. In the process of grain filling, a grain first contains milky liquid, becomes sticky, and then hardens during maturity. Thus, the panicle water content gradually decreases over the ripening stage [7,8]. Indeed, a yellowing color and water content decrease in a panicle are practical indicators of harvest maturity.

Satellite remote sensing is currently utilized for various agricultural monitoring purposes [9,10]. Under current global conditions of rising temperatures, remote sensing techniques offer an essential method for resolving harvest time estimates at the individual paddy field level, particularly since spatial resolutions of satellite imagery data are getting finer. Optical remote sensing and a vegetation index calculated from near infrared and visible bands are utilized in retrieving crop and canopy water contents [11–13]. Radar backscattering in microwave remote sensing is also used for the purpose (reviewed in detail in the following paragraph) [14].

Among these techniques, synthetic aperture radar (SAR) is vital in monitoring the Earth's surface under cloud cover. Although the sensor maintains a solid capacity to capture images without sunlight in almost all-weather conditions, high revisit capabilities required for monitoring crops with shorter growth durations were not achieved until the operation of Copernicus Sentinel-1 satellites. Sentinel-1A and -1B were launched in 2014 and 2016, respectively, carrying C-band SAR sensors operated at a high-frequency equivalent to a wavelength of 5.5 cm for observation. Accordingly, many agricultural studies have employed Sentinel-1 data for agricultural land mapping [10,15–17], as well as yield estimation and crop growth monitoring [18–20]. The Sentinel-1 uses an interferometric wide (IW) mode mostly with VV and VH dual polarizations in land observation, where V and H refer to vertical and horizontal polarization, and the first and second characters denote the transmitted and received polarization, respectively.

Various studies have monitored seasonal changes in SAR backscatter parameters and compared them with in situ data, including vegetation structural parameters. Accordingly, the general relationship between C-band polarimetric parameters and plant growth conditions has been relatively well characterized; however, analyses targeting rice crops [15,20–22] should be different from those assessing wheat and maize [16,18,19,23–28], as the inundated ground surface in such irrigated systems creates a unique environment in signal backscatter.

Microwaves are sensitive not only to the moisture content in vegetation and soil but also to vegetation structures and surface roughness beneath the vegetation as well [25,29]. Moreover, Henderson and Lewis [29] found that senescence and plant maturity reduce the water content, thereby increasing microwave penetration into the plant body. Some studies have attempted to define the precise relationships between vegetation water content and backscatter, as these constitute critical components to understanding crop conditions [23,25,27,28]. Backscatter parameters of VV and VH are important. Besides, several studies have utilized a polarization ratio calculated using VV and VH, known as the cross-ratio, which reflects vegetation water content [25,27,28,30]. However, little is known about the relationships between panicle water content in rice crops and C-band backscatter. One essential feature of rice crops is that the plant and panicle gradually dehydrate during the grain-filling period when caryopses develop [7]. To this end, herein, rice crop growth was monitored using C-band Sentinel-1 satellite data to identify a definite relationship between C-band backscatter and panicle water content. The result of this research will be helpful to estimates of panicle water content, which is crucial information for obtaining proper harvest timing.

2. Datasets

2.1. Study Area

A rice paddy field in Saku city, Nagano prefecture, Japan, was used for analysis (Figure 1). Notably, Nagano has been ranked in the top three prefectures of Japan over the past 12 years in terms of yield per 10 acres and percentage of first-class rice in the nation. The rice plant (*Oryza sativa* L. japonica “Koshihikari”), which is the most widely grown and popular cultivar

in Japan, accounts for the 80–90% of all paddies in the study area, and “Akitakomachi” variety with cold resistance mainly grows in a higher altitude region [30]. Furthermore, rice cultivation is a major activity in Saku, with all paddy fields using irrigation systems.

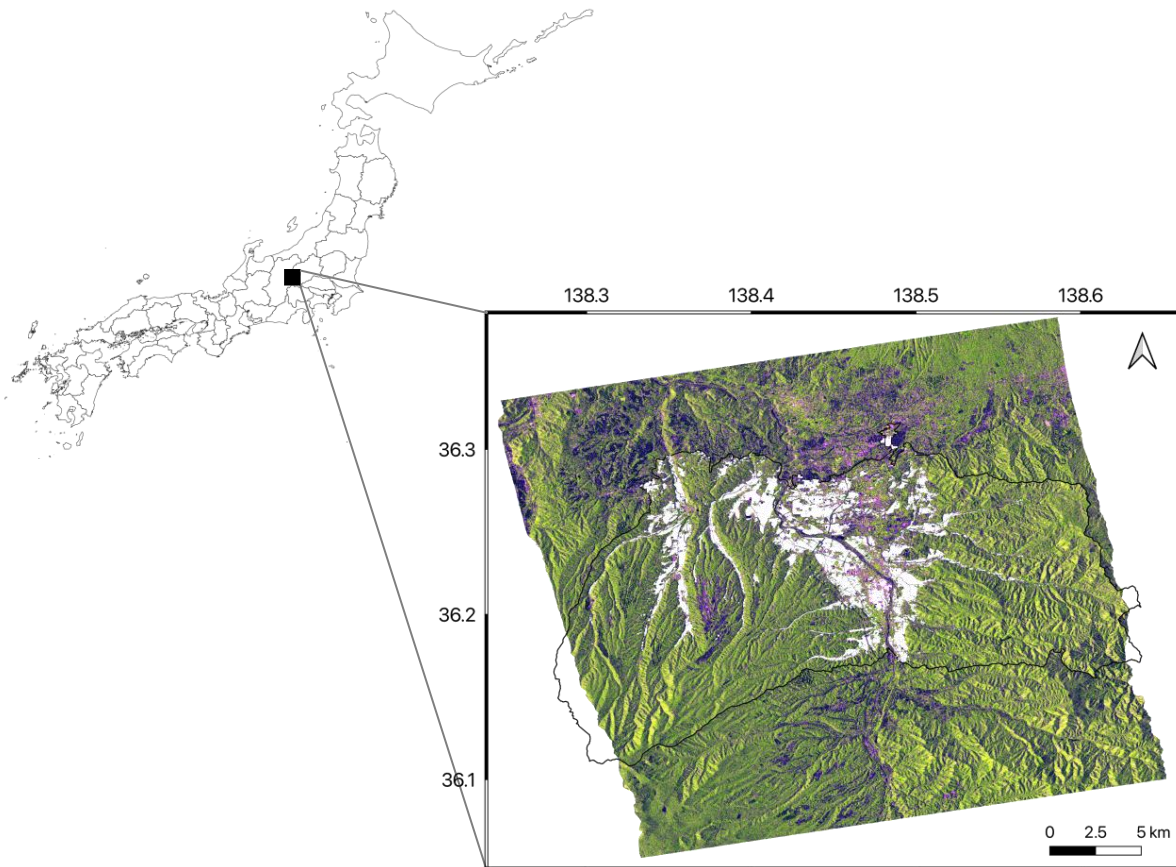


Figure 1. A rice paddy field in Saku city, Nagano Prefecture, Japan, was employed as the study area. White lines show the paddy field; the background image is a color composite of Sentinel-1 data (R: VV, G: VH, B: VV/VH).

Figure 2 depicts an average crop calendar of rice cultivation. In general, transplanting commences from mid-May to early June, with a tillering stage in June and July, and the maximum tiller number stage occurs around mid-July. The heading period generally starts in early August, concluding by mid-August. Following a grain-filling period in September, harvesting typically occurs between late September and early October and ends in mid-October for all paddy fields.

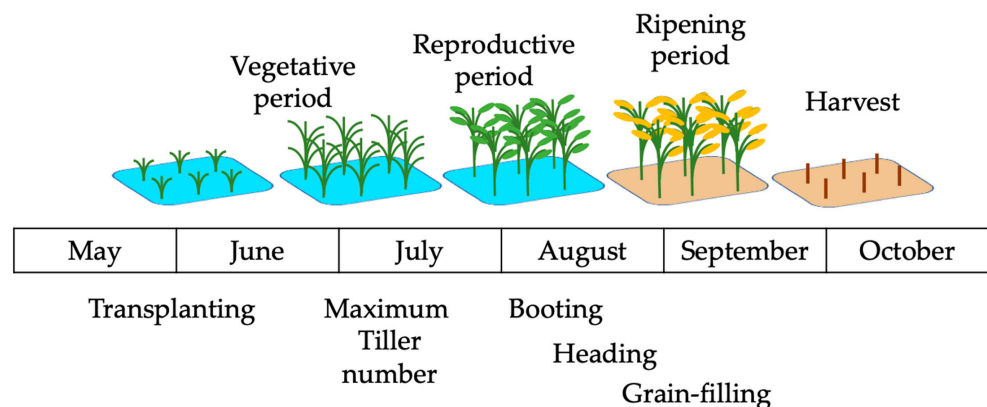


Figure 2. Rice crop calendar in Saku, Nagano, Japan.

2.2. Satellite Remote Sensing Data and Data Processing

Here, Sentinel-1 C-band data were used, taken in both ascending and descending orbits between 2017 and 2020 during the periods of rice crop cultivation (Table 1). Approximately 15 scenes were acquired in one orbit between May to mid-October. All data were Level-1 Single Look Complex (SLC) products, taken in IW mode with VV and VH dual polarizations. The spatial resolution is 2.3 m (range direction) and 13.9 m (azimuth direction). Two orbit datasets, relative orbit number 39 (orb 39; ascending) and 46 (orb 46; descending) were used here (Table 1). Scene acquisition times were 17:41 and 05:43 JST (08:41 and 20:43 UTC) for orb 39 and orb 46, respectively. Since the satellite in orb 39 did not acquire data for this area during August 2018, orb 39 data for 2018 were excluded from the analysis.

Table 1. Field observation dates and Sentinel-1 data acquisition dates. Relative orbit 39 did not acquire scenes in August 2018; hence, orbit 39 data were not analyzed for this year. For field observations, leaf water content measurements were commenced on 2 July 2020, and panicle water content measurements on 22 August 2020. IW1 and IW3 are the numbers of sub-swath. IW1 is the closest to the satellite orbit, and IW3 is the furthest.

Field Observation Date	Ascending Rel_Orb39, Sub-Swath IW1 Incidence Angle 35–36°			Descending Rel_Orb46, Sub-Swath IW3 Incidence Angle 45–46°			
		May 03, 2020	May 09, 2019	May 07, 2017	May 09, 2020	May 03, 2019	May 08, 2018
	May 15, 2020	May 21, 2019	May 19, 2017	May 21, 2020	May 15, 2019	May 20, 2018	May 13, 2017
	May 27, 2020	June 02, 2019	May 31, 2017	Jun. 02, 2020	May 27, 2019	Jun. 01, 2018	May 25, 2017
Jun. 08, 2020	Jun. 08, 2020	Jun. 14, 2019	Jun. 12, 2017	Jun. 14, 2020	Jun. 08, 2019	Jun. 13, 2018	Jun. 06, 2017
	Jun. 20, 2020	Jun. 26, 2019	Jun. 24, 2017	Jun. 26, 2020	Jun. 20, 2019	Jun. 25, 2018	Jun. 28, 2017
Jul. 02, 2020	Jul. 02, 2020	Jul. 08, 2019	Jul. 06, 2017	Jul. 08, 2020	Jul. 02, 2019	Jul. 07, 2018	Jun. 30, 2017
Jul. 14, 2020	Jul. 14, 2020	Jul. 20, 2019	Jul. 18, 2017	Jul. 20, 2020	Jul. 14, 2019	Jul. 19, 2018	Jul. 12, 2017
	Jul. 26, 2020	Aug. 01, 2019	Jul. 30, 2017	Aug. 01, 2020	Jul. 26, 2019	Jul. 31, 2018	Jul. 24, 2017
Aug. 04, 2020	Aug. 07, 2020	Aug. 13, 2019	Aug. 11, 2017	Aug. 13, 2020	Aug. 07, 2019	Aug. 12, 2018	Aug. 05, 2017
Aug. 22, 2020	Aug. 19, 2020	Aug. 25, 2019	Aug. 23, 2017	Aug. 25, 2020	Aug. 19, 2019	Aug. 24, 2018	Aug. 17, 2017
Aug. 30, 2020	Aug. 31, 2020	Sep. 06, 2019	Sep. 04, 2017	Sep. 06, 2020	Aug. 31, 2019	Sep. 05, 2018	Aug. 29, 2017
Sep. 07, 2020	Sep. 12, 2020	Sep. 18, 2019	Sep. 16, 2017	Sep. 18, 2020	Sep. 12, 2019	Sep. 17, 2018	Sep. 10, 2017
Sep. 14, 2020	Sep. 24, 2020	Sep. 30, 2019	Sep. 28, 2017	Sep. 30, 2020	Sep. 24, 2019	Sep. 29, 2018	Sep. 22, 2017
Sep. 21, 2020	Oct. 06, 2020	Oct. 12, 2019	Oct. 10, 2017	Oct. 12, 2020	Oct. 06, 2019	Oct. 11, 2018	Oct. 04, 2017
Sep. 28, 2020	Oct. 18, 2020	Oct. 18, 2019	Oct. 22, 2017	Oct. 24, 2020	Oct. 18, 2019	Oct. 23, 2018	Oct. 16, 2017

Two orbit data taken via different incident angles were expected to be able to observe surface conditions more precisely because of their differences in radar penetration. In orb 39, the scene covers all the paddy fields, and the incidence angle is 35–36°, as the targeted area position is at the end of IW1 sub-swath and close to the IW2 sub-swath. Meanwhile, the orb 46 scene covers two-thirds of the eastern side of the area and is located at the end of the IW3 sub-swath, with an incidence angle of 45–46°.

Data processing was conducted according to the following procedures [31]: precise orbit file and thermal noise corrections were applied for SAR calibration before sub-swath images were merged. The concatenated image was utilized for geometric correction to be projected as Japan Plane Rectangular coordinate system VIII with a pixel spacing of 5 m. Speckle filtering was not applied to preserve original information in the analysis with a small target. Propriety of the filtering processing is application-dependent [32], and previous research on targeted crop fields did not apply it [33,34]. This study disregarded radiometric and geometric terrain corrections, as the paddy fields were situated in flat areas for irrigation system use. Following the data pre-processing, VV and VH radar backscatter powers were converted to sigma naught (σ^0) in decibel units (dB). Hereafter, σ^0_{VV} and σ^0_{VH} are referred to as VV and VH. A polarization ratio of VV/VH (cross-ratio) was then calculated using VV and VH backscatter power rather than logarithmically-transformed dB values.

3. Methods

3.1. Field Observations

Ten paddy fields cultivating “Koshihikari” rice plant were selected to carry out field observations between June and September 2020 (Figure 3a; Table 1, leftmost column). Transplanting was carried out on 14–15 May in six paddies out of 10, 24 May in three paddies, 7 July in one paddy, and harvesting was on 13–20 September in one paddy, 22–27 September in one paddy, and 29 September–4 October in eight paddies. The targeted field maintained an average area of 1835 m² (range: 975–3175 m²). Four stationary observation points, with a square size of 1 m × 1 m, were set at the four corners of each paddy field (Figure 3b). Although these corner observations may not accurately reflect the remaining field sites, the central part of the plots were inaccessible, as local farmers managed the area for production.

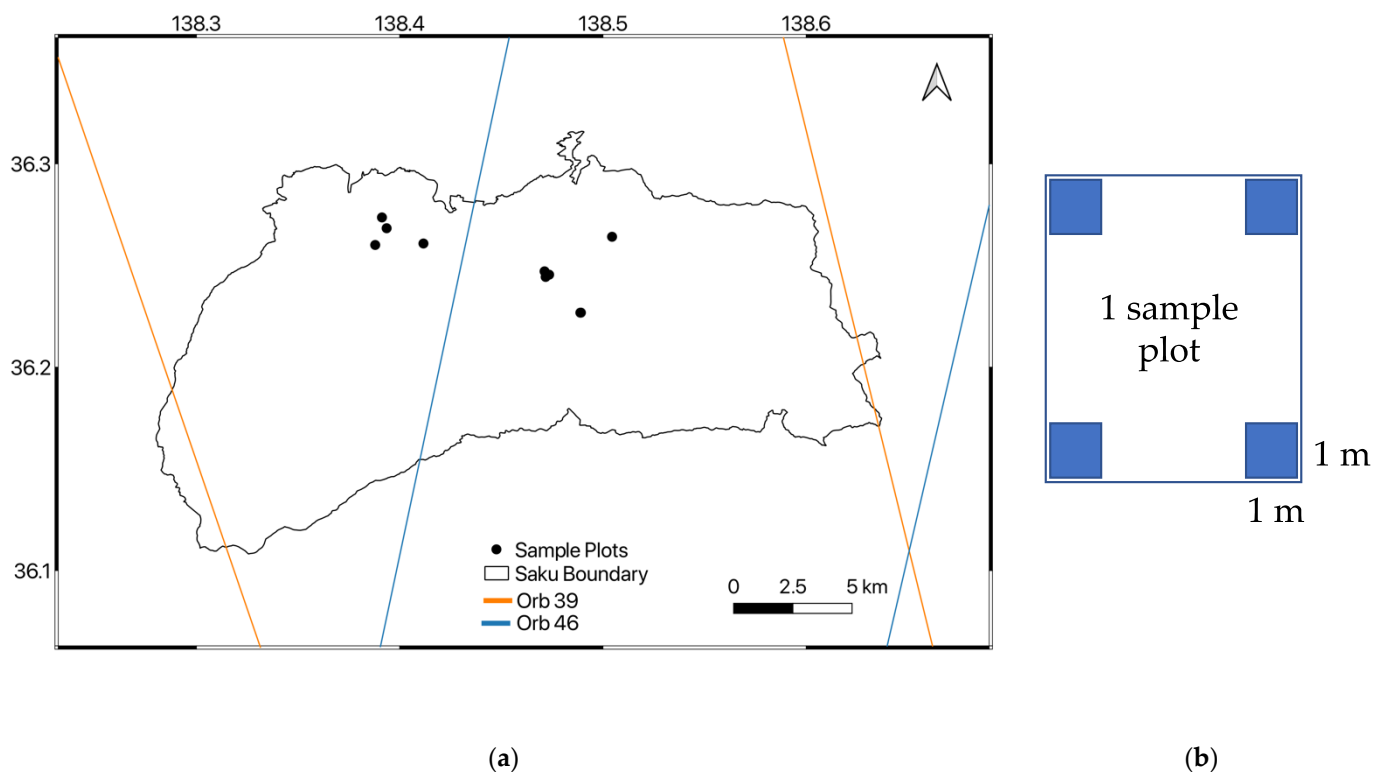


Figure 3. (a) Black circles indicate the locations of the 10 sample plots in Saku. The black line depicts the city boundary. Orange and blue solid lines indicate a swath width of orbit 39 and 46, respectively. (b) Four observation points with square sizes of 1 m² set in each paddy field of the sample plot.

Three tillers per observation point were randomly selected for measurement and averaged within the sample plots; thus, each sample plot had 12-time observations (3 tillers times × 4 sample points) on each observation date. Field observation parameters contained plant height (cm), maximum leaf width (mm), stem number per hill, as well as relative leaf and panicle water content (%). Plant height was measured from the ground surface to the tip of the longest leaf or panicle [35,36]. The stem number in this study refers to the number of several main culms and tillers that arise from the base of the main culm. With regards to vegetation water content, leaves and panicles were separately collected for measuring raw wet and dry weight [23]. Leaf water content was measured from July at the end of a vegetative period, whereas panicle water content measurement commenced in mid-August, when all paddy fields were nearly in the ripening stage. The natural drying method (about six months) was used to calculate relative water contents. Notably, this is the simplest drying method and does not require special facilities [37]. However, it requires a long drying time (three to six months) and

is affected by meteorological factors. This study used the simple method due to our limited access to the facility.

For a more precise analysis, the boundaries of the observed paddy field were digitized on Google Earth, which has a positioning accuracy of 4.7 m in flat areas of Japan [38], so as to delineate the polygon line inside the actual boundary to reduce positional errors and not to include paths between paddy fields. Paddy field boundaries were projected to Japan Plane Rectangular coordinate system VIII in accordance with Sentinel-1 data. Rainfall data were obtained from the Automated Meteorological Data Acquisition System (AMEDAS), operated by the Japan Meteorological Agency. Notably, Saku has one AMEDAS point.

3.2. Seasonal Change in C-Band Backscatter with Rice Crop Growth

The analysis was divided into two parts: monitoring changes in backscatter overall rice crop fields in Saku and statistically investigating how vegetative components affect C-band radar backscatter (discussed further in Section 3.3).

To delineate seasonal changes, a multi-temporal analysis was used to investigate changes in a C-band radar backscatter over the paddy fields (area > 1600 m²). The bottom limit of 1600 m², or 40 m × 40 m, is probably effective to capture seasonal fluctuations in the backscatter because the average area of all 24,500 paddies is 1650 m². There were 11,568 and 8900 paddies greater than 1600 m² in orb 39 and 46 scenes, respectively. Vector polygon data of paddy field boundaries covering the entire area were provided by the Ministry of Agriculture, Japan. The polygon data is updated once a year based on satellite information. A pixel value of VV, VH, and VV/VH within the paddy field were extracted, and the Grubbs test was applied to eliminate outliers for computing the average values of each radar parameter in each paddy field [39]. Changes in the backscatter were monitored for both orbits from one year to the next. The transplant timing as well as harvest timing is different among paddies, ranging over about a month (see Section 2.1). In addition, the same rice plant variety is not cultivated; however, a variety of “Koshihikari” covers 80–90% of paddies. Although there is a difference in the transplanting date, the considerable sample size can compensate for the situation to demonstrate the general seasonal change.

3.3. Statistical Analysis between Field Observations and Satellite Remote Sensing Data

The second analysis intended to determine how vegetation and ground conditions affected radar backscatter; multivariate linear regression was applied to analyze C-band radar backscatter with field observation data, where field-observed vegetation metrics were the explanatory variable and each radar’s parameters (VV, VH, and VV/VH) were the response variable.

The parameters (VV, VH, VV/VH) were extracted on a pixel basis from each of the 10 paddies where field observation was carried out. Afterward, the Grubbs test was applied to eliminate outliers [39] and to calculate the averaged value in each paddy. Before the regression analyses, explanatory variables were converted to z-score values to assist with comparisons between the calculated explanatory coefficients of the regression formula. High correlative relationships between explanatory variables: (i.e., multicollinearity) were tested before the multivariate regression analyses by calculating the diagnosis value of the variance inflation factor (VIF). The explanatory variables which showed the highest VIF values among them were excluded until all VIF values became less than 10 [40], and multivariate analyses incorporated only those remaining variables. Furthermore, the regression analyses employed a stepwise forward selection method to select explanatory variable sets that showed the lowest Akaike’s Information Criterion (AIC) values. Finally, multivariate regressions were conducted with the chosen explanatory variable selected based on VIF criteria and AIC selection.

The multivariate regression analyses were performed separately for: (1) tillering stages before heading in June and July and (2) reproductive and ripening stages in August and September (Figure 2). Orb 39 (ascending) and orb 46 (descending) data were analyzed separately in each period, as their incidence angles were distinct. The three explanatory variables of the regression analyses were plant height, maximum leaf width, and stem number, as water content data were unavailable during the vegetative period. On the other hand, the analysis in the ripening stage used all five-vegetation metrics, which contained water content measurements in leaf and panicle in addition to the three parameters. Remote sensing and field measurement observation dates were not perfectly aligned (Table 1). Accordingly, the closest two remote sensing data before and after each field observation date were used for comparison, the remote sensing dates with no or low rainfall were then selected after assessing AMEDAS rainfall data. Given that the microwave signal is extremely sensitive to water content, the approach was necessary to avoid the impacts of water adhering to the plant surface on radar backscatter.

In one field, transplanting was on 7 June 2020, and Sentinel-1 acquired data on 8 June 2020, when VV and VH were relatively extremely high. Thus, paddy fields within 2–3 days after transplanting are likely to cause remarkably higher backscatter; parcels relevant to the condition were excluded from the analysis.

4. Results

4.1. Overall Growth Monitoring Analysis

4.1.1. Field Observational Data

Figure 4 shows the plant structural parameters (plant height, leaf width, and stem number; Figure 4a), and vegetation water contents in leaves and panicles (Figure 4b). All plot values were averages of the 10 sample plots (Figure 3a) for each parameter. Plant height steadily increased from May to mid-August up to ~110 cm, slightly decreasing after that due to grasshoppers feeding on leaf tips after September. Intensive feeding usually takes place near the end of the harvesting period. Maximum leaf width widened until June up to a relatively constant size of 10–11 mm. Stem number per hill constantly increased up to ~30 stems, during the vegetative period, somewhat decreasing after mid-July before stabilizing (Figure 4a).

Notably, water contents decreased in both leaves and panicles (Figure 4b). Specifically, leaf water content decreased from 80% to 65%, whereas panicle water content sharply declined from 60% to <30% over the grain-filling period. The results of water content data on 30 August 2020, were deemed invalid (e.g., >100%), and were thus excluded from the analysis. This may have been due to heavy rains on this date ($36.5 \text{ mm}\cdot\text{day}^{-1}$, compared to a 30-year average monthly precipitation of $106 \text{ mm}\cdot\text{month}^{-1}$ based on AMEDAS data archives). Furthermore, the sudden rise in water content, or large dispersion in leaf and panicle water contents observed on 7 September 2020, were also likely related to rainwater adhering to the vegetation surface, as the weather data recorded for 5–6 September 2020, showed daily precipitation values of 15.5 mm and 24.5 mm, respectively.

As shown in Figure 4b, a large dispersion was found on 7 September 2020. However, we included it in further analysis. The reason was as follows. The panicle water contents were measured starting from 22 August. Unfortunately, the second observation on 30 August had no validity, showing >100% of the water contents, and was disregarded from the analysis. If we further excluded the data on 7 September, about 3 weeks were left between the first and second observations. Therefore, to maintain statistical validity, we included the data on 7 September to prioritize keeping the sample size.

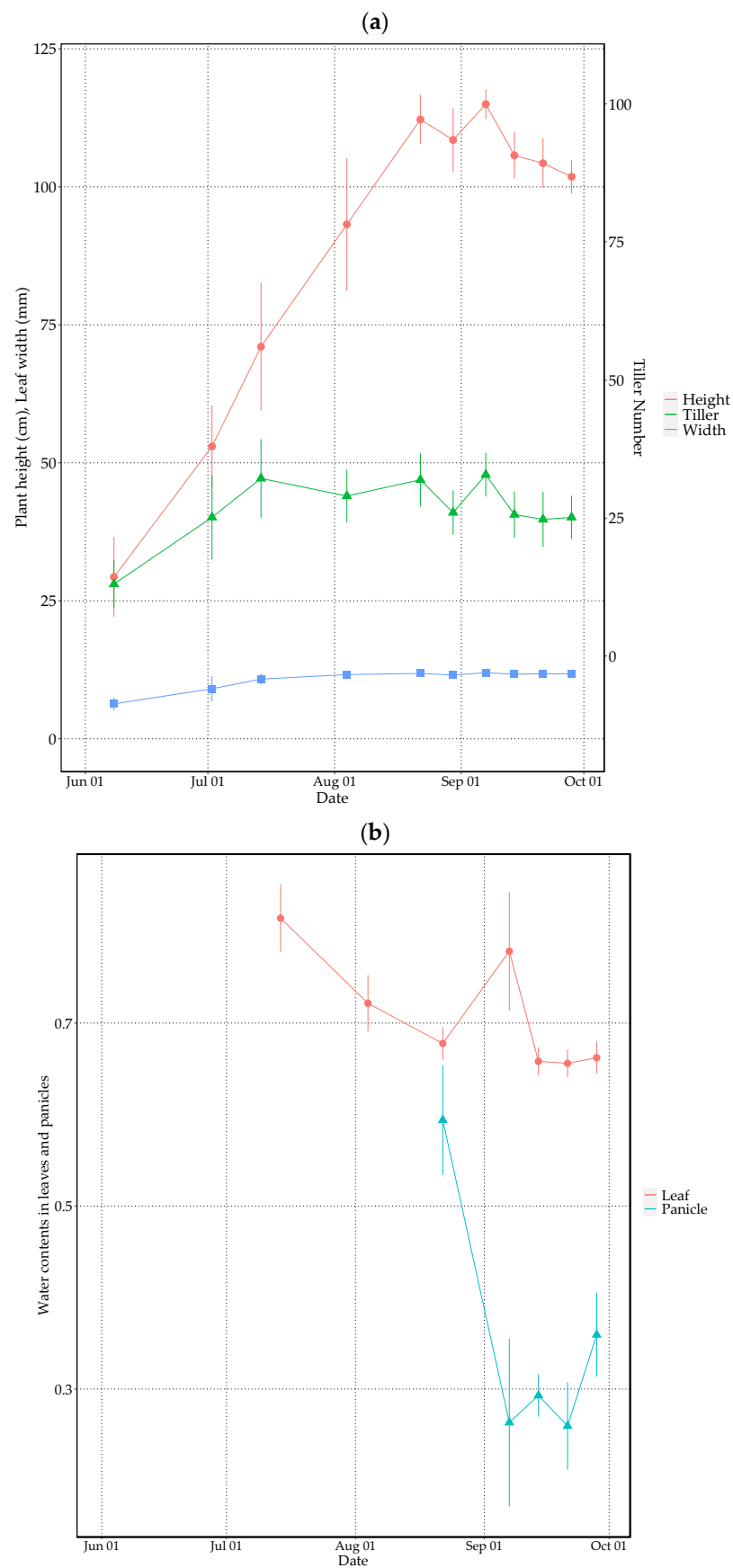


Figure 4. Field observation data for: (a) plant height (cm), maximum leaf width (mm), stem number per hill, and (b) water contents of leaves and panicles.

4.1.2. Changes in Sentinel-1 Radar Backscattering

Figure 5 shows time-series changes in VV (σ^0_{VV}), VH (σ^0_{VH}), and VV/VH for 2020 (Figure 5a), 2019 (Figure 5b), 2018 (Figure 5c), and 2017 (Figure 5d).

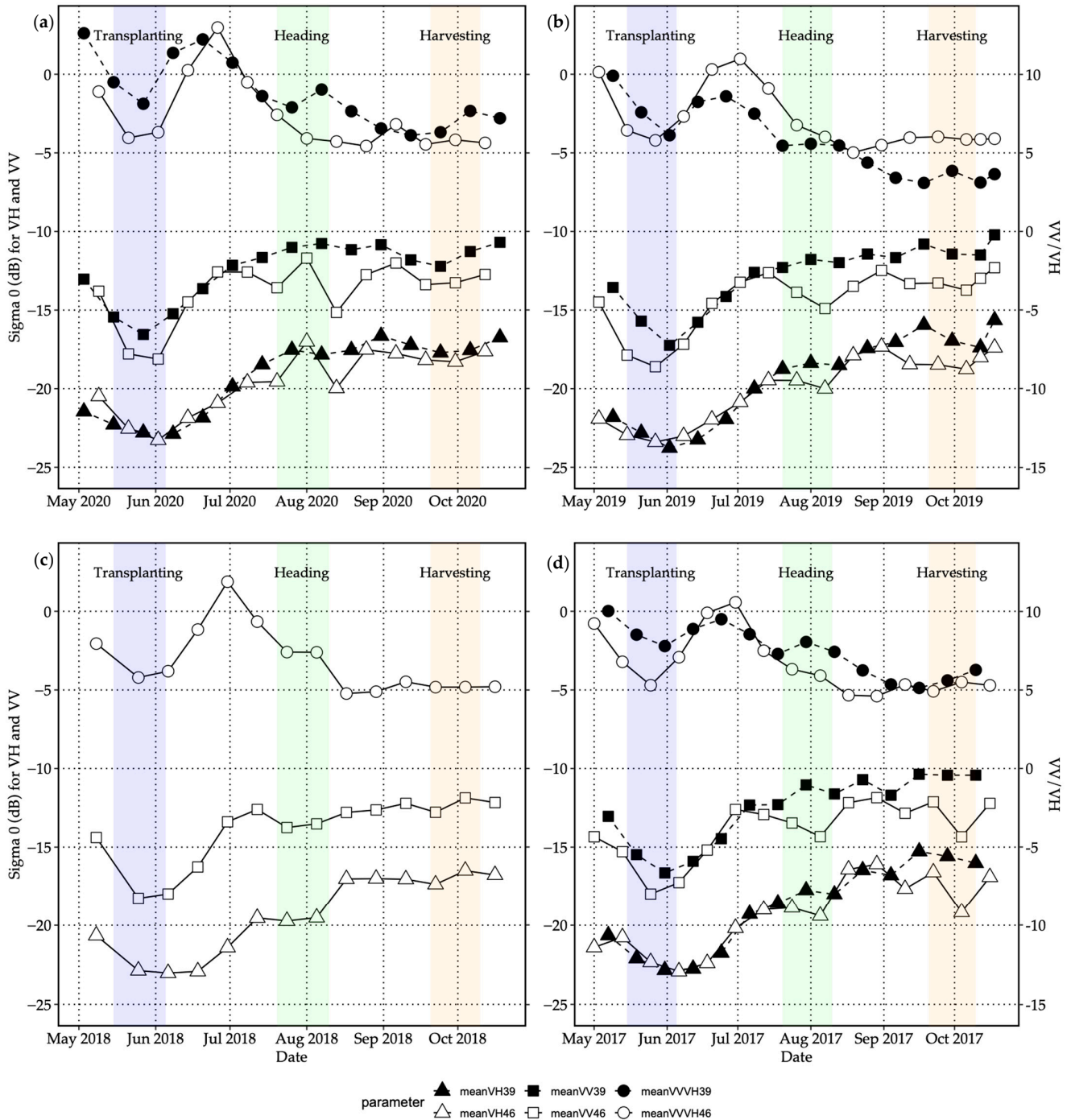


Figure 5. Time-series changes in σ^0_{VV} (triangles), σ^0_{VH} (squares), and VV/VH (circles) for (a) 2020, (b) 2019, (c) 2018, and (d) 2017 for orb 39 (solid) and orb 46 (blank). Data in orb 39 were missing in 2018; thus, they were excluded from the analysis.

Seasonal changes in radar backscatter showed similar tendencies among analysis years. All three parameters sharply decreased in early June during the middle of the transplanting period, followed by a steady increase during the first stages of the vegetative period in June (Figure 2). In July, VV/VH significantly decreased, whereas VV and VH

increased continuously. Over August and September, VV and VH in orb 46 fluctuated substantially, whereas orb 39 data seemed to slightly increase; whereas VV/VH in orb 46 appeared stable, they continually decreased in orb 39. Post-harvest in October, VV and VH slightly increased.

4.2. Multivariate Regression Analysis

The results of multivariate linear regression analysis for each vegetative and ripening period are in Tables 2 and 3.

Table 2. Results of the multivariate linear regression analysis. Selected variables are shown with coefficients and p -values in parenthesis, a hyphen “-” indicates that the variable is not selected by the AIC method. The overall accuracy of the selected model was evaluated with Adj. R^2 and p -value are shown in parenthesis. Data in orb 39 (ascending) and 46 (descending) were analyzed separately for the vegetative period (June and July). Leaf and panicle water contents were not observed during the vegetative period.

Vegetative Period (June and July)		Coefficients and p -Value (in Parentheses) of AIC Selected Explanatory Variables (x)				
		Height	Leaf Width	Stem Number	Adj. R^2	
Response variables(y)	Orb 39	VH	2.276 (0.001)	-	-	0.397 (0.001)
		VV	-	-	0.853 (0.051)	0.136 (0.051)
		VV/VH	-	-	-	-
	Orb 46	VH	-	-	0.628 (0.002)	0.507 (0.002)
		VV	-3.823 (0.134)	-	2.398 (0.073)	0.126 (0.177)
		VV/VH	-5.786 (0.113)	-	2.755 (0.139)	0.062 (0.270)

Table 3. Results of the multivariate linear regression analysis. Selected variables are shown with coefficients and p -values in parenthesis; a hyphen “-” indicates that the variable is not selected by the AIC method. The overall accuracy of the selected model was evaluated with Adj. R^2 and p -value are shown in parenthesis. Data in orb 39 (ascending) and 46 (descending) were analyzed separately for the reproductive and ripening periods (August and September).

Reproductive & Ripening Periods (August and September)		Coefficients and p -Value (in Parentheses) of AIC Selected Explanatory Variables (x)						
		Height	Leaf Width	Stem Number	Leaf Water	Panicle Water	Adj. R^2	
Response variables (y)	Orb 39	VH	-2.425 (0.160)	-	-	-	0.042 (0.160)	
		VV	-	-	-	0.828 (0.027)	0.155 (0.027)	
		VV/VH	-	-	1.381 (0.106)	-	2.128 (<0.001)	0.405 (<0.001)
	Orb 46	VH	-	-3.656 (0.219)	-	0.869 (0.089)	-1.402 (0.002)	0.607 (0.002)
		VV	4.232 (0.109)	-	-	-	-3.352 (<0.001)	0.741 (<0.001)
		VV/VH	-	-	-	-	-1.892 (0.021)	0.277 (0.021)

The coefficients and p -values for each explanatory variable selected based on AIC values and adjusted R^2 value (Adj. R^2) calculated with the selected variables are also shown. Scatterplots display the relationships between vegetation and microwave backscatter parameters and are shown separately for the vegetative periods of orb 39 (Figure 6) and orb 46 (Figure 7), as well as the ripening periods of orb 39 (Figure 8) and orb 46 (Figure 9).

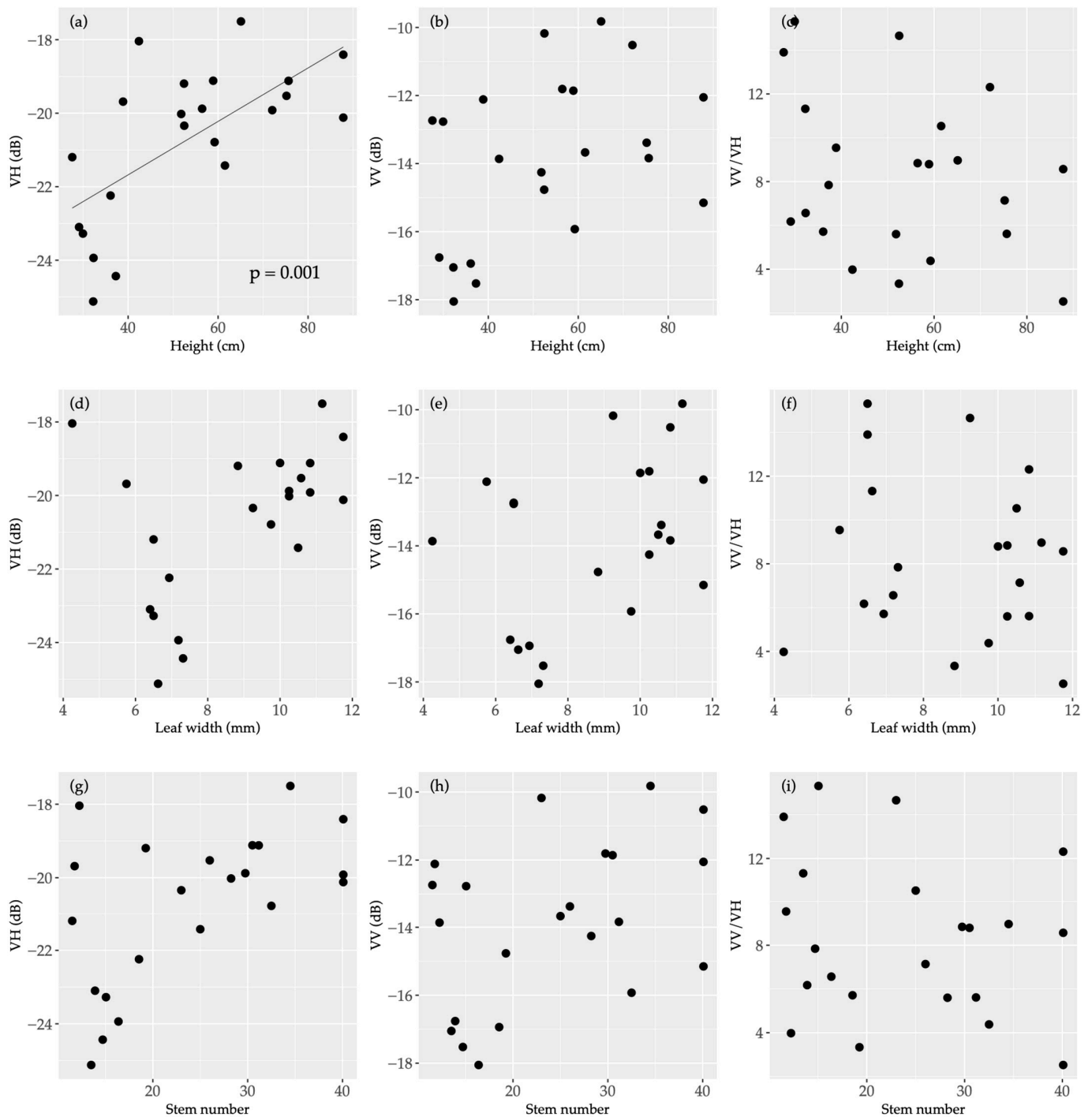


Figure 6. Scatterplots of field-observed biophysical parameters in the vegetative stage and microwave backscatter values from orb 39. Plant height (cm), maximum leaf width (mm), and stem number were measured in the tillering stage. The leftmost column depicts VH, the center shows VV, and the rightmost presents VV/VH. (a–c) plant height, (d–f) maximum leaf width, and (g–i) stem number, respectively.

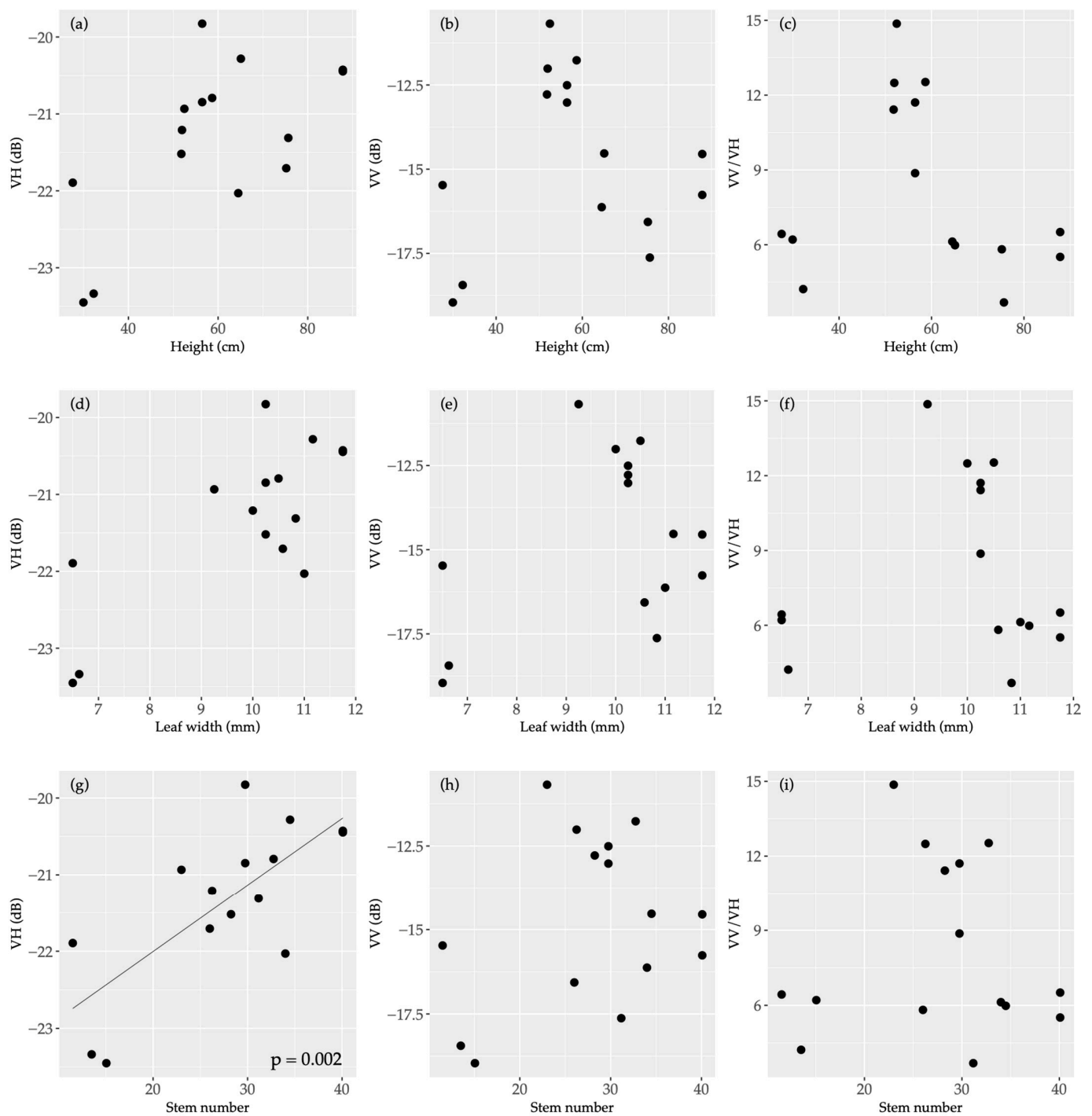


Figure 7. Scatterplots of field-observed biophysical parameters in the vegetative stage and microwave backscatter values from orb 46. Plant height (cm), maximum leaf width (mm), and stem number were measured in the tillering stage. The leftmost column depicts VH, the center shows VV, and the rightmost presents VV/VH. (a–c) plant height, (d–f) maximum leaf width, and (g–i) stem number, respectively.

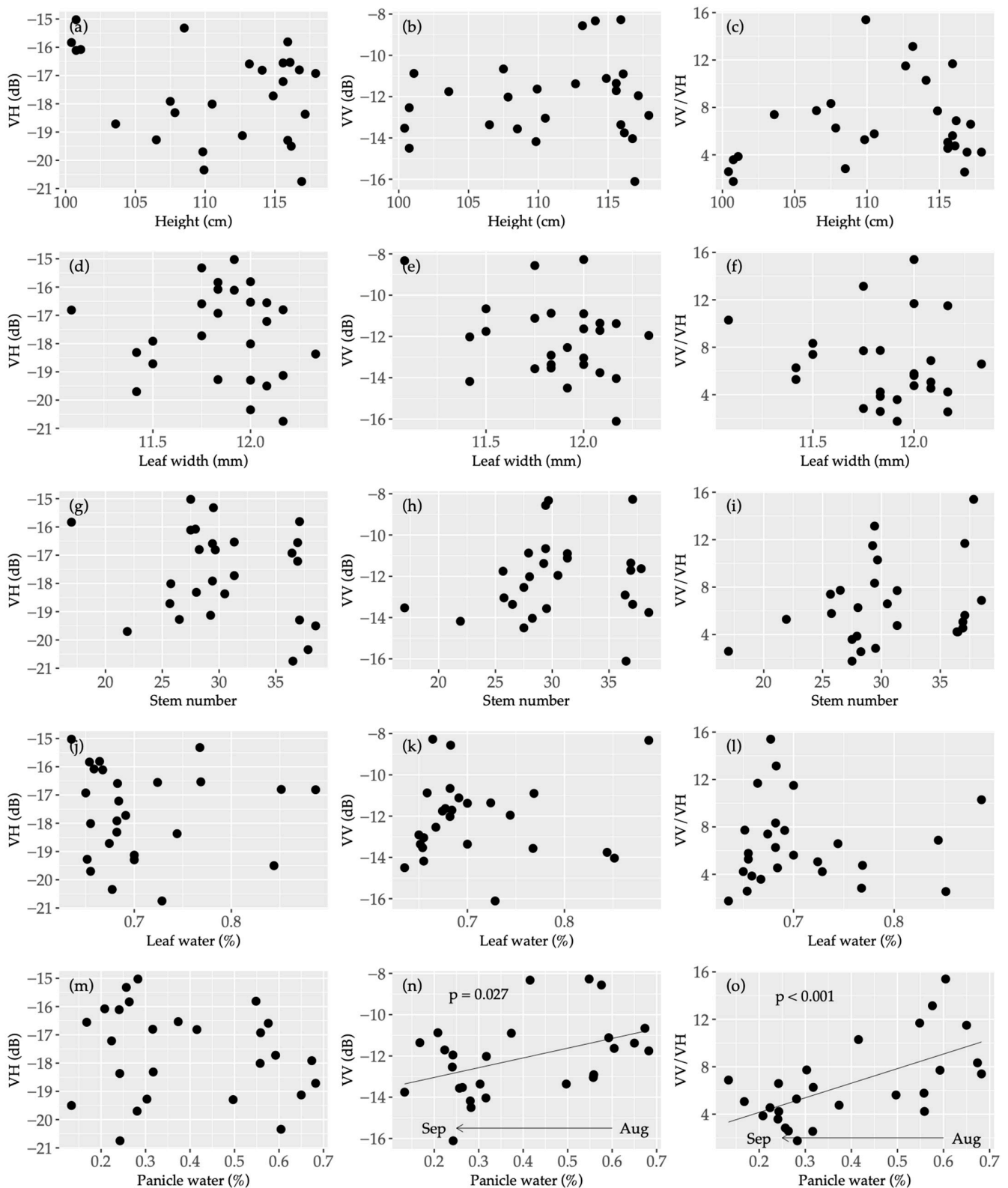


Figure 8. Scatterplots of biophysical parameters during reproduction and ripening periods and microwave backscatter values from orb 39. Plant height (cm), maximum leaf width (mm), stem number, and water content in leaves and panicles (%) are field measurement data. The leftmost column depicts VH, the center shows VV, and the rightmost presents VV/VH. (a–c) plant height, (d–f) maximum leaf width, (g–i) stem number, (j–l) leaf water content, and (m–o) panicle water content respectively.

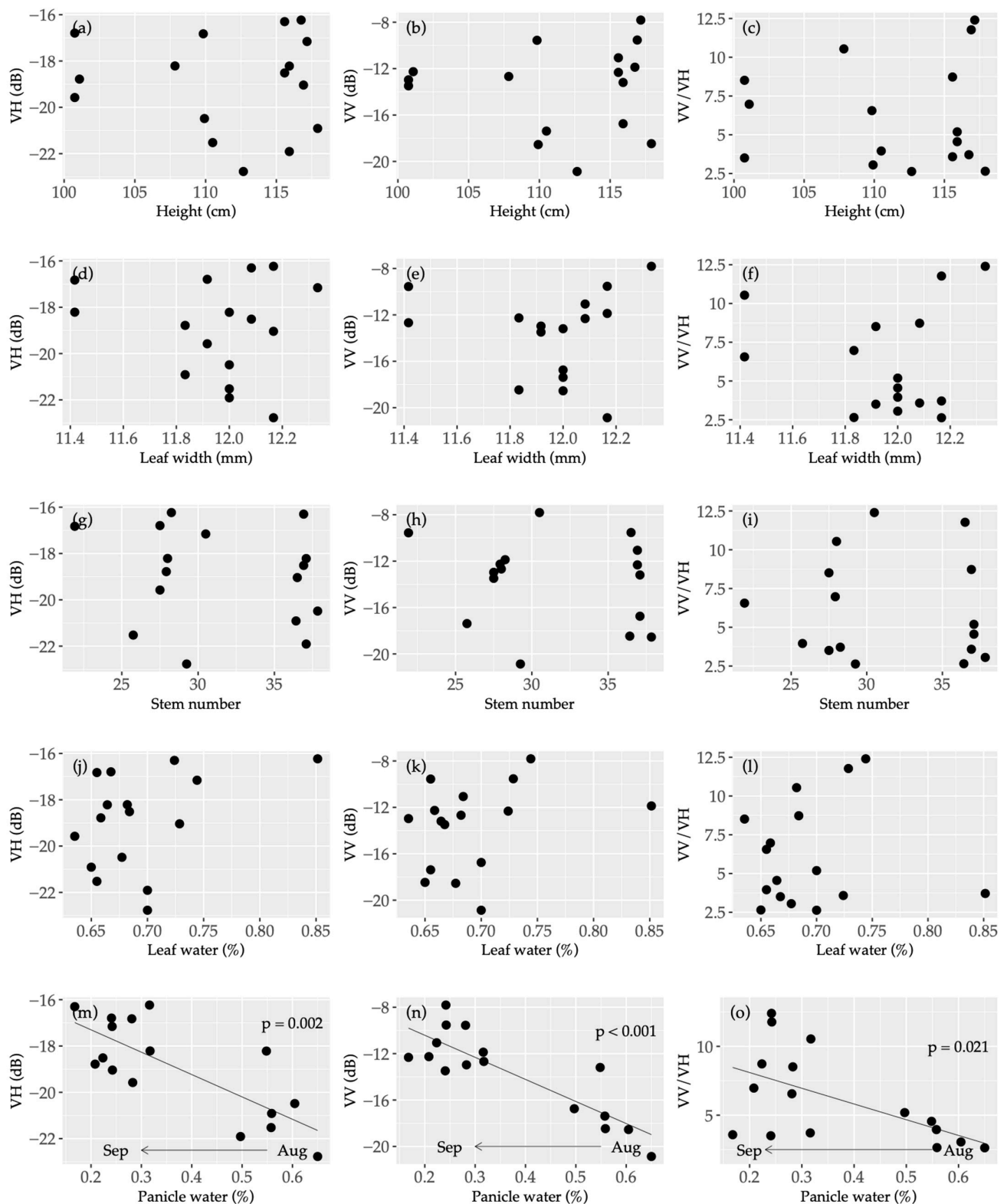


Figure 9. Scatter plots between biophysical parameters during reproduction and ripening periods and microwave backscatters taken in orb 46. Plant height (cm), maximum leaf width (mm), stem number, and water content in leaves and panicles (%) are field measurement data. The leftmost column depicts VH, the center shows VV, and the rightmost presents VV/VH. (a–c) plant height, (d–f) maximum leaf width, (g–i) stem number, (j–l) leaf water content, and (m–o) panicle water content respectively.

In the vegetative period (Table 2), the VIF values were 6.05, 7.75, and 9.15 for plant height, leaf width, and stem number, respectively. Notably, no multicollinearity was observed. Accordingly, all three variables were used in the regression analysis. VH in orbs 39 and 46 showed significantly positive correlations with height (Adj. $R^2 = 0.397$, $p = 0.001$; Figure 6a), and stem number (Adj. $R^2 = 0.507$, $p = 0.002$; Figure 7g), respectively; by contrast, the other parameters of VV and VV/VH showed no significant correlations with vegetation parameters ($p > 0.05$).

During the reproductive and ripening periods (Table 3), the VIF values were 2.68, 1.46, 1.98, 1.70, and 1.34 for plant height, leaf width, stem number, leaf water content, and panicle water content, respectively, with no multicollinearity observed between them. Accordingly, all five variables were used in the regression analysis. In orb 39, VH showed no significant correlation; whereas VV displayed a relatively weak positive correlation with only panicle water content (Adj. $R^2 = 0.155$, $p = 0.027$; Figure 8n), VV/VH showed strong positive correlations (Adj. $R^2 = 0.405$, $p < 0.001$) with panicle water content ($p < 0.001$; Figure 8o) and stem number ($p = 0.106$; Figure 8i). In orb 46, all polarimetric values showed high correlations with vegetation parameters; VH maintained a strong correlation (Adj. $R^2 = 0.607$, $p = 0.002$) with panicle water content ($p = 0.002$, Figure 9m), leaf water content ($p = 0.089$; Figure 9j), and leaf width ($p = 0.219$; Figure 9d), whereas VV had a significant correlation (Adj. $R^2 = 0.741$, $p < 0.001$) with panicle water content ($p < 0.001$; Figure 9n) and height ($p = 0.109$; Figure 9b). VV/VH maintained a higher correlation only with panicle water content (Adj. $R^2 = 0.277$, $p = 0.021$; Figure 9o). In particular, panicle water content showed significant negative correlations with all the C-band backscatter parameters in orb 46 (Table 3).

5. Discussion

5.1. Rice Crop Growth

The observation data of biophysical parameters (Figure 4) showed consistency with the previous works [8,41]. It is well established that plant height undergoes a sharp increase during the vegetative stage and continues to increase even during the reproductive stage due to culm elongation [8]. Growth stops after the heading, which occurs between early to mid-August in the study area. As seen in the present study, the stem number steadily increased until ~60 days after transplanting, slightly decreasing thereafter before approaching quasi-stability. As a native plant characteristic, a tiller that is not eared is dried to transfer water and nutrients into the panicles; thus, the number after the maximum tillering period and during the booting stage is consequently decreased. Therefore, stem number decreases after early July when the maximum tiller number is reached, as stems without their heads wither.

Leaf water contents gradually decreased after the maximum tillering stage and continued to decrease until the harvest period; however, these decreases were relatively small compared with those in the panicle. One previous study [42] also observed a slight reduction in leaf water content throughout the growth period. Conversely, panicle water content suddenly decreased from ~60% to 25% during the ripening stage. We utilized the simple natural drying method to obtain relative water contents; however, the value is consistent with the previous works. Iwaya and Yamamoto [43] conducted experiments in Japan's rice paddies to show a similar decreasing tendency, with results in the water content decreasing from 59% to 18%. They also indicated that the panicle water content at the harvest time ranged from ~20% to 25%. Furthermore, Yoshida [8] showed that changes in the grain water content varied from 58% in the initial grain-filling period to 20% during maturity.

5.2. Seasonal Changes in Backscattered Microwave according to Rice Crop Growth

The temporal behavior of backscatter over rice crops observed here (Figure 5) was very similar to that seen in previous studies [15,44]. Bazzi et al. [15] demonstrated that the behavior of VV/VH showed a Gaussian bell shape between rice transplanting and harvesting periods and was markedly different from other crops, such as maize and wheat.

Moreover, compared to VV and VH, the ratio parameter (VV/VH) in both orbs 39 and 46 appeared to mitigate the impacts of atmospheric water vapor to lessen backscatter fluctuation and derive smoother line graphs. Veloso et al. [27] also indicated that the ratio can reduce the influence of some environmental factors (e.g., soil moisture), to achieve more stable results. Consequently, using the VV/VH ratio makes it easier to observe the seasonal changes in microwave backscatters.

Backscatter behavior for each of the growing stages analyzed can be summarized as follows:

- **Transplanting period:** Backscatters in both VV and VH showed a clear decrease in early June, at the end of the transplanting period. The low backscatter values here are most likely related to the specular reflection of the irrigated water surface [45]. After the transplanting, a water depth of about 3–4 cm is kept until the seedling takes root, and the tips of the seedling leaves can only be seen on the water surface. Therefore, the surface condition immediately after planting is similar to a flat-water surface, which generates low backscattered signals. However, paddy fields within 2 or 3 days after transplanting showed markedly high backscatter values, likely caused by a ridge appearing on the water surface created by the rice transplanting machine. Accordingly, the C-band SAR data taken in the days following transplantation should be excluded from the analysis.
- **Vegetative period:** The results uniquely demonstrated that VV/VH increased in the early tillering stage before suddenly decreasing in the latter tillering stage. This finding indicates that VV in the early stage increased more rapidly than VH because of the steady increase in plant height (Figure 4a). As a basic scattering mechanism, a vertically polarized microwave is transmitted toward the ground both in VV and VH polarization. When the surface has a vertical component, the received signal becomes stronger in a vertical direction and consists of surface and double-bounce scatterings [46]. Part of the transmitted signal is depolarized by multiple scatterers, such as vegetation, to be received in the orthogonal plane of H [29,47]. The sensitivity of VV to vegetation growth is due to double bounce scattering between plant and water surfaces [48], with the backscatter increasing with larger canopy gaps [49]. Next, the sudden decrease in VV/VH can be explained by the increased stem number and panicle initiation through active tillering. The increased tillers and randomly shaped panicles induce canopy growth to generate backscatter signals in cross-polarization [29] while suppressing the like-polarization backscatter because of microwave attenuation by vertical plant structures [27,29]; thus, the substantial increase in VH leads to the decrease in VV/VH. Previous studies have also illustrated that vegetation growth, as the main scatterer, strongly increases VH and slightly increases VV during the vegetative phase [15,21,22]. The results here showed a similar tendency, additionally revealing a clear inflection point in VV/VH in the middle of the vegetative stage due to the accompanying apparent morphological transformation.

Reproductive and Ripening period: This study demonstrated clear differences in backscatter behavior resulting from different incidence angles, exclusively in this after-heading period. The investigation implies that VV/VH derived at a shallow incidence angle is a superior indicator for diagnosing ripening conditions, which is one of the essential pieces of information for estimating optimal harvest timing. VV/VH in orb 46 is with a shallow incidence angle stopped decreasing during the ripening period; the phenomenon likely related to the following factors: (1) Orb 46 has a shallow incidence angle ($>45^\circ$), indicating that the scattering is strongly affected by crop canopy and panicle condition [27]. Henderson and Lewis [29] specified that shallow incidence angles $>40^\circ$ increased the response from agricultural vegetation; (2) after heading, which ends by the mid-August, the ripening stage begins and results in the small morphological changes, and then the spikelet dries out as it approaches the grain-filling period. These minor structural changes and drying lead to a more gradual backscatter increase in VV and VH to stabilize VV/VH.

Meanwhile, VV/VH with a steeper incidence angle (35–36°) continually decreased from the late vegetative period until harvesting (although a small peak was observed in early August), presumably due to shifting surface conditions from water to soil following water drainage from paddy fields. Changes in surface conditions make VV weaker than VH, as the former is more substantially affected by the surface [27]. Drainage usually commences 30–40 days after heading and 10 days before harvesting (late September in this area). In summary, over the grain-filling period, VV/VH with a shallow incidence angle stopped decreasing due to senescence, whereas it continued decreasing at a steep angle due to water drainage application.

5.3. Statistical Analysis between Ground Observation and C-Band Backscattering

The multivariate linear regression analysis revealed the more robust capacity for panicle water content estimation from C-band imagery taken at a shallow incidence angle. Polarimetric parameters in orb 46, especially VV and VH, showed significant negative correlations to panicle water content (Table 3), indicating that backscatter in VV (Figure 9n) and VH (Figure 9m) increased with senescence—in other words, decreased panicle water content. VV/VH also shows a negative correlation, meaning that VV substantially increased rather than VH. From August to September, the panicle water contents decreased suddenly from 60% to <30%. This lower water content increased microwave penetration into the vegetation [28,29], resulting in increased backscatter values from panicles at shallower incidence angles. Similarly, Khabbazan et al. [25] concluded the VV markedly increased and VH/VV decreased during the senescence stage.

Alternatively, although both VV and VV/VH at a steep incidence angle showed strong positive correlations with the panicle water content (Figure 8n,o; Table 3), the backscatter likely did not reflect vegetation water content, as it is primarily affected by the surface conditions. Microwave signals with steep incidence angles can easily reach the ground by penetrating the plant canopy; thus, penetration levels increase during plant senescence. In August (the heading period), VV scattering was high and tended to decrease in September approaching harvesting (Figure 8n) due to surface drainage, which commences 30–40 days after heading. As it is pointed by the previous research [46], the inundated surface below the canopy behaves as a strong reflecting surface to produce a double-bounce scattering component. Accordingly, surface drainage time beginning in September changed the surface from water to muddy soil, reducing both VV and VV/VH (Figure 8o). Notably, panicle water content likely synchronizes more closely with surface water content than leaf water content, which did not decrease during the ripening stage (Figure 4b). Previous studies observed a remarkable decrease by 15–20% in soil moisture contents of rice paddies during the ripening stage [50]. The panicle water content showed pseudo-correlations with backscatter values in orb 39.

The results here identified different backscatter behavior between two orbits and were primarily aligned with the findings of Veloso et al. [27], who mentioned that shallow incidence angles (>30–40°) enhanced the impact of vegetation on backscatter values, whereas steeper incidence angles (<30°) were susceptible to ground conditions owing to deeper microwave penetration.

6. Conclusions

In recent years, global warming has impacted agricultural practices and production. Rice crop production also suffers from temperature rise, which causes deterioration of the grain quality. Remote sensing technology is expected to monitor an extensive area of agricultural land to retrieve a biophysical crop parameter. Here, rice crop growth was monitored using Sentinel-1 C-band imagery with high-frequency observations of understanding microwave backscatter behavior as it corresponds to changes in crop phenology, water contents, and surface conditions.

The temporal changes analyses illustrated a similar tendency across all four notable years, although unique variation trends were delineated for each different incidence angle.

The VV/VH ratio at a shallow incidence angle delineated special temporal behavior, no longer decreasing after the heading period and thus becoming stable over the reproductive and ripening periods. The phenomenon is due to both minor morphological changes in crops and the reduction in the panicle water content during the period. The senescent particularly allowed for greater microwave penetration into the canopy, thereby increasing panicle-related backscatter. Furthermore, multivariate regression analysis demonstrated that VV and VH with shallow incidence angles were strongly negatively correlated with panicle water content, demonstrating backscattering increases with decreases in the water contents via senescence.

Thus, it was observed that backscatter behaviors were highly consistent with crop phenological changes, and microwave backscatter information enabled the retrieval of rice crop conditions. Accordingly, data with shallow incidence angles indicated a strong potential for estimating panicle water content. Therefore, it seems reasonable to conclude that C-band SAR data is capable of using for proper harvesting time estimation. The relationship is likely sustained because the backscattered signal with a shallow incidence angle is not greatly affected by the surface to reflect panicle condition. However, further investigation in other areas is essential to generalize the relationship.

Author Contributions: Conceptualization, H.I.; Formal analysis, S.K.; Investigation, H.I.; Writing—original draft, S.K. All authors have read and agreed to the published version of the manuscript.

Funding: This research was funded by College of Agriculture, Tamagawa University. Grant name is “Collaborative Research Grant 2020 in the College of Agriculture, Tamagawa University”. This work was also supported by JSPS KAKENHI Grant Number 18K11626.

Data Availability Statement: Not applicable.

Acknowledgments: I wish to thank Y. KOHAMA (Saku Agricultural and Rural Support Center, Saku, Nagano Pref., Japan) for the kind supports and arrangement for the field observation.

Conflicts of Interest: The authors declare no conflict of interest. The funders had no role in the design of the study; in the collection, analyses, or interpretation of data; in the writing of the manuscript, or in the decision to publish the results.

References

1. Fukagawa, N.K.; Ziska, L.H. Rice: Importance for global nutrition. *J. Nutr. Sci. Vitaminol.* **2019**, *65*, S2–S3. [CrossRef] [PubMed]
2. Karthikeyan, L.; Chawla, I.; Mishra, A.K. A review of remote sensing applications in agriculture for food security: Crop growth and yield, irrigation, and crop losses. *J. Hydrol.* **2020**, *586*, 124905. [CrossRef]
3. The Ministry of Agriculture Forestry and Fisheries of Japan. To Overcome the High Temperature Damage of Paddy Rice. High Temperature Damage Countermeasure Report. Available online: https://www.maff.go.jp/j/kanbo/kihyo03/gityo/g_kiko_hendo/suito_kouon/pdf/report.pdf (accessed on 4 June 2022). (In Japanese)
4. Fahad, S.; Adnan, M.; Hassan, S.; Saud, S.; Hussain, S.; Wu, C.; Wang, D.; Hakeem, K.R.; Alharby, H.F.; Turan, V.; et al. Rice Responses and Tolerance to High Temperature. In *Advances in Rice Research for Abiotic Stress Tolerance*; Woodhead Publishing: Cambridge, UK, 2019; pp. 201–224.
5. Sakaiya, E.; Inoue, Y. Operational Use of Remote Sensing for Harvest Management of Rice. *J. Remote Sens. Soc. Jpn.* **2013**, *33*, 185–199. (In Japanese)
6. Brouwer, C.; Prins, K.; Heibloem, M. *Irrigation Water Management: Irrigation Scheduling; Water Resources, Development and Management Service Land and Water Development Division*; FAO: Rome, Italy, 1989.
7. Morris, M.L. *Rice Production: A Training Manual and Field Guide to Small-Farm Irrigated Rice Production*; Peace Corps, Information Collection and Exchange: Washington, DC, USA, 1980.
8. Yoshida, S. *Fundamentals of Rice Crop Science*; The International Rice Research Institute: Manila, Philippines, 1981.
9. Ishitsuka, N.; Ouchi, K. The Application of Synthetic Aperture Radar to Agriculture. *J. Remote Sens. Soc. Jpn.* **2017**, *37*, 182–192. (In Japanese)
10. Liu, C.-A.; Chen, Z.-X.; Shao, Y.; Chen, J.-S.; Hasi, T.; Pan, H.-Z. Research advances of SAR remote sensing for agriculture applications: A review. *J. Integr. Agric.* **2019**, *18*, 506–525. [CrossRef]
11. Xu, C.; Qu, J.J.; Hao, X.; Cosh, M.H.; Zhu, Z.; Gutenberg, L. Monitoring crop water content for corn and soybean fields through data fusion of MODIS and Landsat measurements in Iowa. *Agric. Water Manag.* **2020**, *227*, 105844. [CrossRef]
12. Han, D.; Liu, S.; Du, Y.; Xie, X.; Fan, L.; Lei, L.; Li, Z.; Yang, H.; Yang, G. Crop water content of winter wheat revealed with Sentinel-1 and Sentinel-2 imagery. *Sensors* **2019**, *19*, 4013. [CrossRef]

13. Pan, H.; Chen, Z.; Ren, J.; Li, H.; Wu, S. Modeling winter wheat leaf area index and canopy water content with three different approaches using Sentinel-2 multispectral instrument data. *IEEE J. Sel. Top. Appl. Earth Obs. Remote Sens.* **2018**, *12*, 482–492. [[CrossRef](#)]
14. Quemada, C.; Pérez-Escudero, J.M.; Gonzalo, R.; Eder, I.; Santesteban, L.G.; Torres, N.; Iriarte, J.C. Remote sensing for plant water content monitoring: A review. *Remote Sens.* **2021**, *13*, 2088. [[CrossRef](#)]
15. Bazzi, H.; Baghdadi, N.; El Hajj, M.; Zribi, M.; Minh, D.H.T.; Ndikumana, E.; Courault, D.; Belhouchette, H. Mapping Paddy Rice Using Sentinel-1 SAR Time Series in Camargue, France. *Remote Sens.* **2019**, *11*, 887. [[CrossRef](#)]
16. Beriaux, E.; Jago, A.; Lucau-Danila, C.; Planchon, V.; Defourny, P. Sentinel-1 Time Series for Crop Identification in the Framework of the Future CAP Monitoring. *Remote Sens.* **2021**, *13*, 2785. [[CrossRef](#)]
17. Chang, L.; Chen, Y.-T.; Wang, J.-H.; Chang, Y.-L. Rice-Field Mapping with Sentinel-1A SAR Time-Series Data. *Remote Sens.* **2020**, *13*, 103. [[CrossRef](#)]
18. Kumar, P.; Prasad, R.; Gupta, D.K.; Mishra, V.N.; Vishwakarma, A.K.; Yadav, V.P.; Bala, R.; Choudhary, A.; Avtar, R. Estimation of winter wheat crop growth parameters using time series Sentinel-1A SAR data. *Geocarto Int.* **2017**, *33*, 942–956. [[CrossRef](#)]
19. Silva-Perez, C.; Marino, A.; Cameron, I. Monitoring Agricultural Fields Using Sentinel-1 and Temperature Data in Peru: Case Study of Asparagus (*Asparagus officinalis* L.). *Remote Sens.* **2020**, *12*, 1993. [[CrossRef](#)]
20. Wali, E.; Tasumi, M.; Moriyama, M. Combination of Linear Regression Lines to Understand the Response of Sentinel-1 Dual Polarization SAR Data with Crop Phenology—Case Study in Miyazaki, Japan. *Remote Sens.* **2020**, *12*, 189. [[CrossRef](#)]
21. He, Z.; Li, S.; Wang, Y.; Dai, L.; Lin, S. Monitoring Rice Phenology Based on Backscattering Characteristics of Multi-Temporal RADARSAT-2 Datasets. *Remote Sens.* **2018**, *10*, 340. [[CrossRef](#)]
22. Ndikumana, E.; Ho Tong Minh, D.; Dang Nguyen, H.; Baghdadi, N.; Courault, D.; Hossard, L.; El Moussawi, I. Estimation of Rice Height and Biomass Using Multitemporal SAR Sentinel-1 for Camargue, Southern France. *Remote Sens.* **2018**, *10*, 1394. [[CrossRef](#)]
23. Harfenmeister, K.; Itzerott, S.; Weltzien, C.; Spengler, D. Agricultural Monitoring Using Polarimetric Decomposition Parameters of Sentinel-1 Data. *Remote Sens.* **2021**, *13*, 575. [[CrossRef](#)]
24. Harfenmeister, K.; Spengler, D.; Weltzien, C. Analyzing Temporal and Spatial Characteristics of Crop Parameters Using Sentinel-1 Backscatter Data. *Remote Sens.* **2019**, *11*, 1569. [[CrossRef](#)]
25. Khabbazan, S.; Vermunt, P.; Steele-Dunne, S.; Ratering Arntz, L.; Marinetti, C.; van der Valk, D.; Iannini, L.; Molijn, R.; Westerdijk, K.; van der Sande, C. Crop Monitoring Using Sentinel-1 Data: A Case Study from The Netherlands. *Remote Sens.* **2019**, *11*, 1887. [[CrossRef](#)]
26. Nasirzadehdizaji, R.; Balik Sanli, F.; Abdikan, S.; Cakir, Z.; Sekertekin, A.; Ustuner, M. Sensitivity Analysis of Multi-Temporal Sentinel-1 SAR Parameters to Crop Height and Canopy Coverage. *Appl. Sci.* **2019**, *9*, 655. [[CrossRef](#)]
27. Veloso, A.; Mermoz, S.; Bouvet, A.; Le Toan, T.; Planells, M.; Dejoux, J.-F.; Ceschia, E. Understanding the temporal behavior of crops using Sentinel-1 and Sentinel-2-like data for agricultural applications. *Remote Sens. Environ.* **2017**, *199*, 415–426. [[CrossRef](#)]
28. Vreugdenhil, M.; Wagner, W.; Bauer-Marschallinger, B.; Pfeil, I.; Teubner, I.; Rüdiger, C.; Strauss, P. Sensitivity of Sentinel-1 Backscatter to Vegetation Dynamics: An Austrian Case Study. *Remote Sens.* **2018**, *10*, 1396. [[CrossRef](#)]
29. Henderson, F.M.; Lewis, A.J. *Principles and Applications of Imaging Radar (Manual of Remote Sensing: Volume 2)*; Wiley: New York, NY, USA, 1998.
30. Yoshihiko, K. *Personal Communication*; Saku Agricultural and Rural Support Center: Nagano, Japan, 2022.
31. Filippini, F. Sentinel-1 GRD preprocessing workflow. *Multidiscip. Digit. Publ. Inst. Proc.* **2019**, *18*, 11.
32. Garrison, J.L. Welcome to the September Issue [From the Editor]. *IEEE Geosci. Remote Sens. Mag.* **2021**, *9*, 3–5. [[CrossRef](#)]
33. Kang, Y.; Özdoğan, M. Field-level crop yield mapping with Landsat using a hierarchical data assimilation approach. *Remote Sens. Environ.* **2019**, *228*, 144–163. [[CrossRef](#)]
34. Yonezawa, C.; Negishi, M.; Azuma, K.; Watanabe, M.; Ishitsuka, N.; Ogawa, S.; Saito, G. Growth monitoring and classification of rice fields using multitemporal RADARSAT-2 full-polarimetric data. *Int. J. Remote Sens.* **2012**, *33*, 5696–5711. [[CrossRef](#)]
35. Anwari, G.; Moussa, A.A.; Wahidi, A.B.; Mandozai, A.; Nasar, J.; El-Rahim, M.G.M.A. Effects of Planting Distance on Yield and Agro-morphological Characteristics of Local Rice (Bara Variety) in Northeast Afghanistan. *Curr. Agric. Res. J.* **2019**, *7*, 350–357. [[CrossRef](#)]
36. Sritarapipat, T.; Rakwatin, P.; Kasetkasem, T. Automatic rice crop height measurement using a field server and digital image processing. *Sensors* **2014**, *14*, 900–926. [[CrossRef](#)]
37. Tomczak, K.; Tomczak, A.; Jelonek, T. Effect of Natural Drying Methods on Moisture Content and Mass Change of Scots Pine Roundwood. *Forests* **2020**, *11*, 668. [[CrossRef](#)]
38. Guo, J.; Zhang, J.X.; Zhao, H.T.; Li, C.; Zhou, J.; Tu, H.J.; Zhao, Y. Horizontal Accuracy Assessment of Google Earth Data over Typical Regions of Asia. *Int. Arch. Photogramm. Remote Sens. Spat. Inf. Sci.* **2020**, *XLIII-B3-2020*, 1333–1338. [[CrossRef](#)]
39. Bonakdari, H.; Zeynoddin, M. *Stochastic Modeling: A Thorough Guide to Evaluate, Pre-Process, Model and Compare Time Series with MATLAB Software*; Elsevier Science: Amsterdam, The Netherlands, 2022.
40. Montgomery, D.C.; Peck, E.A.; Vining, G.G. *Introduction to Linear Regression Analysis*; John Wiley & Sons: Hoboken, NJ, USA, 2021.
41. Feng, Z.; Qi, Z.; Zhang, Z.; Zheng, E.; Yu, J.; Zheng, Y. Effective Tiller Numbers, Photosynthetic and Yield Response of Rice (*Oryza sativa*) to Shallow Wet–Dry Irrigation Water Controlled at Tillering Stage in Black Soil Area. *Agric. Res.* **2020**, *10*, 97–104. [[CrossRef](#)]

42. Nozulaidi, M.; Jahan, M.S.; Khairi, M.; Khandaker, M.M.; Nashriyah, M.; Khanif, Y.M. N-acetylcysteine increased rice yield. *Turk. J. Agric. For.* **2015**, *39*, 204–211. [[CrossRef](#)]
43. Iwaya, K.; Yamamoto, H. The diagnosis of optimal harvesting time of rice using digital imaging. *J. Agric. Meteorol.* **2005**, *60*, 981–984. [[CrossRef](#)]
44. Lasko, K.; Vadrevu, K.P.; Tran, V.T.; Justice, C. Mapping Double and Single Crop Paddy Rice With Sentinel-1A at Varying Spatial Scales and Polarizations in Hanoi, Vietnam. *IEEE J. Sel. Top Appl. Earth Obs. Remote Sens.* **2018**, *11*, 498–512. [[CrossRef](#)]
45. Balz, T.; Soergel, U.; Crespi, M.; Osmanoglu, B. *Advances in SAR: Sensors, Methodologies, and Applications*; MDPI: Basel, Switzerland, 2018.
46. Flores Anderson, A.I.; Herndon, K.E.; Kucera, L.M. *SAR Handbook: Background*; SERVIR Global: Huntsville, AL, USA, 2019.
47. Evans, D.L.; Farr, T.G.; Ford, J.; Thompson, T.W.; Werner, C. Multipolarization radar images for geologic mapping and vegetation discrimination. *IEEE Trans. Geosci. Remote Sens.* **1986**, *GE-24*, 246–257. [[CrossRef](#)]
48. Bouvet, A.; Le Toan, T.; Lam-Dao, N. Monitoring of the rice cropping system in the Mekong Delta using ENVISAT/ASAR dual polarization data. *IEEE Trans. Geosci. Remote Sens.* **2009**, *47*, 517–526. [[CrossRef](#)]
49. Rosenqvist, A.; Killough, B. A Layman's Interpretation Guide to L-band and C-band Synthetic Aperture Radar Data, v2.0. Available online: https://ceos.org/ard/files/Laymans_SAR_Interpretation_Guide_2.0.pdf (accessed on 24 June 2022).
50. Arif, C. Optimizing Water Management in System of Rice Intensification Paddy Fields by Field Monitoring Technology. Ph.D. Thesis, Tokyo University, Tokyo, Japan, 2013.